Spatial wave control using a self-biased nonlinear metasurface at microwave frequencies

MEHDI KIANI,[1] ALI MOMENI,[2] MAJID TAYARANI,[1,*] AND CAN DING[3]

[1]*Department of Electrical Engineering, Iran University of Science and Technology, Tehran 1684613114, Iran*
[2]*Laboratory of Wave Engineering, School of Electrical Engineering, EPFL, Station 11, 1015 Lausanne, Switzerland*
[3]*Global Big Data Technologies Centre, University of Technology Sydney, Ultimo, NSW 2007, Australia*
*m_tayarani@iust.ac.ir

Abstract: Recently, investigation of metasurfaces has been extended to wave control through exploiting nonlinearity. Among all of the ways to achieve tunable metasurfaces with multiplexed performances, nonlinearity is one of the promising choices. Although several proposals have been reported to obtain nonlinear architectures at visible frequencies, the area of incorporating nonlinearity in form of passive-designing at microwave metasurfaces is open for investigation. In this paper, a passive wideband nonlinear metasurface is manifested, which is composed of embedded L−shape and Γ−shape meta-atoms with PIN-diode elements. The proposed self-biased nonlinear metasurface has two operational states: at low power intensities, it acts as a Quarter Wave Plate (QWP) in the frequency range from 13.24 GHz to 16.38 GHz with an Axial Ratio (AR) of over 21.2%. In contrast, at high power intensities, by using the polarization conversion property of the proposed PIN-diode based meta-atoms, the metasurface can act as a digital metasurface. It means that by arranging the meta-atoms with a certain coding pattern, the metasurface can manipulate the scattered beams and synthesize well-known patterns such as diffusion-like and chessboard patterns at an ultra-wide frequency range from 8.12 GHz to 19.27 GHz (BW=81.4%). Full-wave and nonlinear simulations are carried out to justify the performance of the wideband nonlinear metasurface. We expect the proposed self-biased nonlinear metasurface at microwave frequencies reveals excellent opportunities to design limiter metasurfaces and compact reconfigurable imaging systems.

1. Introduction

At the beginning of the century, remarkable attention was absorbed to metasurfaces as the sub-wavelength structures owing to their electromagnetic features, besides being low loss and easy to chip. Metasurfaces have created a broad area to wave control from microwave to optical frequencies. Meanwhile, theoretical developments like the emergence of Generalized Snell's law of reflection and refraction, paved this way. The result of the rapid growth of metasurfaces to wave control has witnessed and found a special place in achieving negative refraction [1,2], engineered antennas [3–5], beam scanning [6], invisibility cloak [7,8], absorbers [9], polarizers [10], dispersion engineering [11,12], and advanced analog computing [13–17]. Demands for any type of flexible structures made scientists of this field use the materials like graphene [18–20], vanadium dioxide [21–23] and semiconductors [24,25] as the phase change materials. In addition to the use of unique materials to obtain metasurfaces with different functionalities, nonlinearity can also help to achieve controllable metasurfaces. In recent years, especially at visible frequencies by using diverse nonlinear materials, several numbers of studies have incorporated nonlinearity into the metasurface design for many applications such as polarization rotation [26], harmonic generation [27], frequency multiplexing [28], and so forth. More recently,

at microwave frequencies, with the help of semiconductor lumped elements like PIN-diodes and varactors which embedded into the unit cells, active power-dependent metasurfaces have been presented. Varactors at different powers can display different behaviors, and the power levels verify the capacitance of them in each time [24]. On the other side, PIN-diode at low power intensities acts as an open circuit or more precisely like a small capacitance, and at high power intensities when the power intensity is more than a specified threshold, it operates as a short circuit or small resistance [29]. Sievenpiper's group in 2013 by introducing a high power surface wave circuit-based metasurface absorber [30] opened new doors to reach reconfigurable metasurfaces through the use of the nonlinear property at microwave frequencies. Digital coding metasurfaces have created an opportunity to spatially re-distribute scattered waves via two distinct coding meta-atoms with opposite reflection/transmission phases (e.g., 0° and 180°) as the "0" and "1" digital bits form the metasurface [31–33]. More recently, Cui's group proposed two intensity-dependent metasurfaces whose functionality of them have been determined by the power intensity of the incoming wave [34,35]. Organizing coding particles with the help of varactor elements into the metasurface give them an opportunity to control scattered waves spectrally and spatially. In fact, "digital coding" and "nonlinearity" has emerged as a fascinating paradigm due not only to their capabilities of digitally manipulating EM waves, but also to synthesizing a metasurface with multiplexed performances.

However, these nonlinear metasurfaces control the state of the integrated semiconductor lumped elements with DC bias networks. In such metasurfaces using bias networks increases the complexity of the systems, dramatically. One idea to solve this problem is biasing integrated lumped elements with AC input signals; this approach for embedded PIN-diodes in various microwave devices has been experimentally studied in many works [36–38]. In 2017 [38], a frequency selective surface (FSS) was introduced to provide passband for high power intensities which could spectrally manipulate incoming wave; despite the previous nonlinear metasurfaces, the PIN-diodes have been biased with AC signals and no bias network had been employed in the FSS. However, this FSS could only control the incoming wave spectrally.

Recently a self-biased dual-band nonlinear metasurface has been proposed by authors [39] which at low power functions like an EM-mirror, while at high power levels shows two separate camouflage behaviors at C- and X-band. However, similar to the other previous works, they achieve restricted functionalities at low power state, and moreover the operating band of the digital metasurface was limited to a single narrow frequency region that is unattractive for power limiting applications.

In this paper, an ultrawideband self-biased nonlinear metasurface is presented, comprising of two types of nonlinear power-multiplexed L− shape and Γ− shape meta-atoms. At low-power intensities, the metasurface acts as a QWP that means it converts Linear Polarized (LP) waves to Circular Polarized (CP) waves at low-power state. By contrast, at high power intensities, the metasurface acts as a Digital Spatial Wave Manipulator Metasurface (DSWMM) by reflecting the LP incoming wave in cross-polarization and owing to deploying two nonlinear anti-phase meta-atoms. Indeed, the integrated PIN-diodes in the meta-atoms directly interact with the incoming wave and all its functionalities is solely dictated by the power intensity of the incident wave. Hence, our metasurface synthesizing is fully passive, it does not require any additional active biasing network, and, moreover, its performances are wideband enough for a wide diversity of practical applications demanding protection of sensitive devices from undesired high power signals. The numerical simulations verify the performance of the proposed bi-functional nonlinear coding metasurface.

2. Theory of analysis and design

2.1. Principle and design

Figure 1 shows a perspective view of the nonlinear metasurface, which is composed of L−shape and Γ−shape PIN-diode integrated meta−atoms. The overall geometry of the proposed metasurface is described in Figs. 2(a) and 2(b) consisting of three layers: 1) the L-shape metallic part as the top layer, 2) a 3.683 mm RT/duroid 5880 substrate, and 3) a copper ($\sigma = 5.96 \times 10^7$ S/m) ground plane as the bottom layer to zero transmission. The PIN-diode can be circuitously modelled as an RL-circuit (L=30 pH, R=7.8 Ω) in the on-state while it can be represented by an LC-circuit (L=30 pH, C=0.028 pF) in the off mode [40]. The common structural parameters of the proposed meta-atom are p=10.6 mm, w_x=2.1 mm, w_y=1.5 mm, l_d=0.6 mm, l_y=6.6 mm, and l_x=4.2 mm. By changing the power intensity of the incoming wave, the electromagnetic responses of the proposed metasurface can be tailored, leading to a QWP at low power intensities and a DSWMM at high power intensities. At low power intensities, when PIN-diodes are in off-state and electric field vector slanted 45°relative to both x− and y−directions the metasurface acts as a QWP. However, upon illuminating by high-power radiations, the functionality of the proposed device is changed; the metasurface can reflect LP waves to cross-polarized waves such that the L−shape and Γ−shape meta−atoms mimic the digital states "0" and "1", realizing specific coding pattern over the surface. The operational principle of the aforementioned metasurface is based on the circuit model of the PIN-diode which is changed from an LC-circuit to RL-circuit through increasing the power level of the illuminating wave. It is clear that the voltage levels induced on both ends of the embedded diode powerfully rely on the local field intensities stimulated by different incident power levels. Therefore, Depending on the induced voltage levels of PIN-diodes, we will see different electromagnetic responses. At low power illuminations, the peak of the induced voltage of PIN-diodes is not high enough to turn them on, therefore, they are modelled as open circuits (off-state) or more precisely as LC-circuits. Conversely, at high power illuminations, when the induced voltage of PIN-diodes is more than the threshold, they act as short circuits (on-state) or more accurately as RL-circuits [41](see Fig. 2(c)). In spite of the previous metasurface
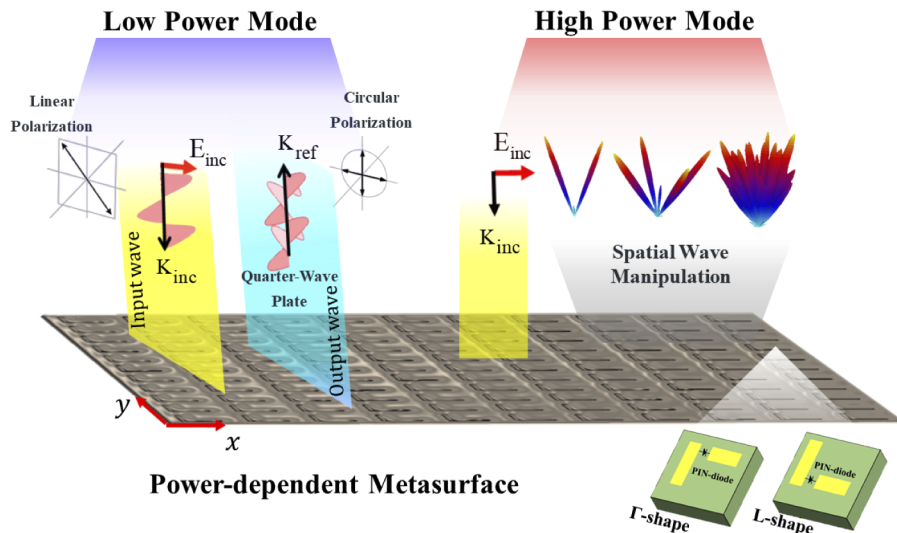

Fig. 1. The perspective view of the nonlinear metasurface. When a weak tilted linear-polarized wave is incident to the metasurface, it acts as a quarter-wave plate. Whenever a high power wave is illuminated the metasurface, the operational status changes to a 1-bit digital metasurface.

demonstrations [34,35,42], the proposed nonlinear metasurface controls the off- and on-states of the PIN-diode without any auxiliary biasing network so that the operational status of the diodes is dictated by the power intensity of the incident wave. During the time variations of the high power AC illuminating signal, majority carriers (holes of P-type and electrons of N-type semiconductors) are stored in the intrinsic layer of PIN-diodes. Since the recombination time of the majority carriers as the off-to-on switching speed (that depends upon the resistivity and permittivity of the semiconductors and is typically on the order of a few picoseconds) has a close value to the input signal cycle, the PIN-diode in the off-mode can follow the AC signal, and switch from off-state to on-state. Meanwhile, at low frequencies, because recombination time of minority carriers (holes of N-type and electrons of P-type semiconductors) as the on-to-off switching speed of the diode are in the order of time-domain signal period (for the exploited PIN-diode it is 2 nS), the stored charges can be detached from the intrinsic layer; therefore, the diode can switch to off mode. Conversely, at high frequencies, the recombination time of the minority carriers has a considerable value against the period of the input signal (if we consider the frequency range of simulations between 10 to 20 GHz, the corresponding time periodicity range will be T=50 ps to 100 pS; in this case, switching speed at least 20 times are bigger than the time periodicity.) Consequently, there is not sufficient time to switch off the PIN-diode, and at high power illuminations, the PIN-diode will work stably in the on-state [41]. One important issue that must be considered when choosing a PIN-diode is that the operating frequency of the metasurface must be in the useable frequency range of the PIN-diodes; here the operating frequency range of the metasurface is 8 GHz to 20 GHz that is in the useable frequency range of the MADP-000907-14020.
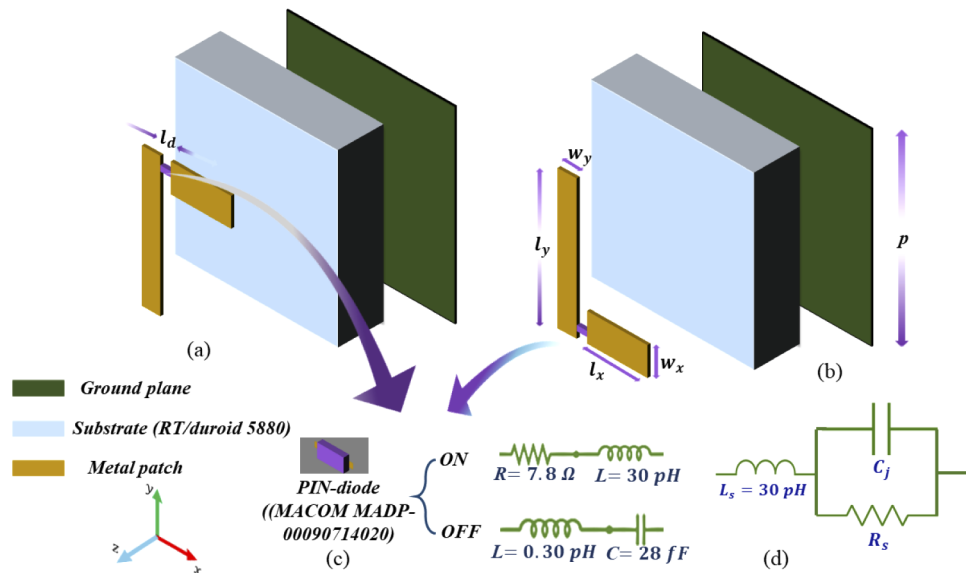

Fig. 2. (a), (b) The Γ−shape and L−shape meta−atoms as the basic units of the metasurface. (c) circuit model of the embedded PIN-diodes for on- and off-states. (d) SPICE model of the PIN-diode.

2.2. Frequency-domain analysis

To study the performance of the proposed metasurface. we consider that it is illuminated by a travelling wave along the z−direction; the reflected wave can be described as the sum of two LP

components:

$$\vec{E}^r = E_0(\Gamma_x \vec{x} + \Gamma_y \vec{y}) \qquad (1)$$

in which, E_0 is the magnitude of the incident wave in both x- and y-directions. Also, $\Gamma_x = |\Gamma_x|e^{\varphi_x}$ and $\Gamma_y = |\Gamma_y|e^{\varphi_y}$ are the reflection coefficients of E_x^i and E_y^i, respectively The metasurface comprising the proposed meta-atoms (see Fig. 2) as an anisotropic-surface manifests distinct EM responses to the $x-$ and $y-$polarized incident waves, which would be evident in different Γ_x and Γ_y. When the electric field of the incident LP wave is tilted at 45° relative to the $x-$axis, such that the phase difference of the reflected wave $\Delta\varphi_{xy} = 90°$ and $|\Gamma_x| = |\Gamma_y|$, a QWP can be produced. On the other hand, when a $y-$polarized ($x-$polarized) wave illuminates a metasurface so that the reflected wave be in $x-$axis ($y-$axis), a linear-to-linear polarization converter will be achieved. The scattering parameters of the proposed metasurface at different power levels in addition to the distribution of the L−shape and Γ-shape meta−atoms determine the electromagnetic performance of the metasurface. Here, the functionality of the metasurface as a QWP at low power levels and DSWMM at high power levels is investigated by using the commercial program, CST Microwave Studio. Periodic boundary conditions in $x-$ and $y-$directions along with Floquet ports assigned in $z-$ direction form an infinite array from the meta-atoms of Figs. 2(a) and 2(b). At low power levels, as illustrated in Fig. 1, the metasurface is illuminated by a 45° tilted plane wave and plays the role of a QWP; in this case, PIN-diodes are in off-state and they are replaced by $LC-$circuits in the full-wave simulator. Figure 3(a) shows the simulated reflection coefficients and phase delay of the QWP. At low power levels, the metasurface as the QWP presents a reflection coefficient more than −3 dB and phase delay 90° ± 10° from 13.24 GHz to 16.38 GHz for both of $L-$ and Γ−shaped meta-atoms. This means that the metasurface converts the LP incident wave to a CP wave in the reflection mode.

In contrast, when the nonlinear meta-atoms are exposed to high-power plane waves, digital EM response is observable. In fact, when the power level of $y-$polarized incident wave is increased, the PIN-diodes change their states from off-to-on. In the full-wave simulator, they are replaced with RL-circuits (see Fig. 2). Therefore, the function of the metasurface is switched to an LP-to-LP polarizer. Figure 3(b) depicts the co- and cross-polarized reflection spectra for the infinite array of L−shape and Γ−shape upon illuminating by $y-$polarized plane waves. In which, $\Gamma_{xy} = E_x^r / E_y^i$ and $\Gamma_{yy} = E_y^r / E_y^i$ indicate the reflection coefficients of the y-to-x and y-to-y polarizations, respectively. The cross-polarized reflection coefficient Γ_{xy} is higher than −1.5 dB in an ultra-wide frequency band from 8.12 GHz to 19.27 GHz, while the co-polarized reflection coefficient Γ_{yy} is lower than −10 dB in this frequency range. Hence, at high power intensities, the proposed meta-atoms can efficiently convert an LP wave into cross-polarization. As illustrated in Fig. 3(c) at high power levels, there is a 180° phase difference between L−shape and Γ−shape meta−atoms. Consequently, they can be considered as "0" and "1" binary codes. Actually, the binary phase response required for constructing the coding metasurface is acquired at the wideband frequency range.

In this study to justify the circuit models performance that are employed in the full-wave simulator, a nonlinear simulation setup in ADS software was established where the SPICE model of the PIN-diodes had been used. In ADS with the help of the LSSP control palette, the Hot S Parameters (large-signal scattering parameters) were computed and reported in Fig. 3. In fact, the Hot S Parameters are the scattering parameters of the structure when the SPICE model (nonlinear model) of the diodes are exploited. As we can see in Fig. 3, the Hot S parameters (dash-dotted line) and S parameters (solid lines) that are achieved by inserting circuit models in the metasurface, are in good agreement.

To investigate the capacity of the proposed nonlinear anisotropic metasurface in manipulating the polarization states of reflected waves at different power levels, we calculated axial ratio (AR) for circular polarization conversion at low power levels and polarization conversion ratio (PCR)
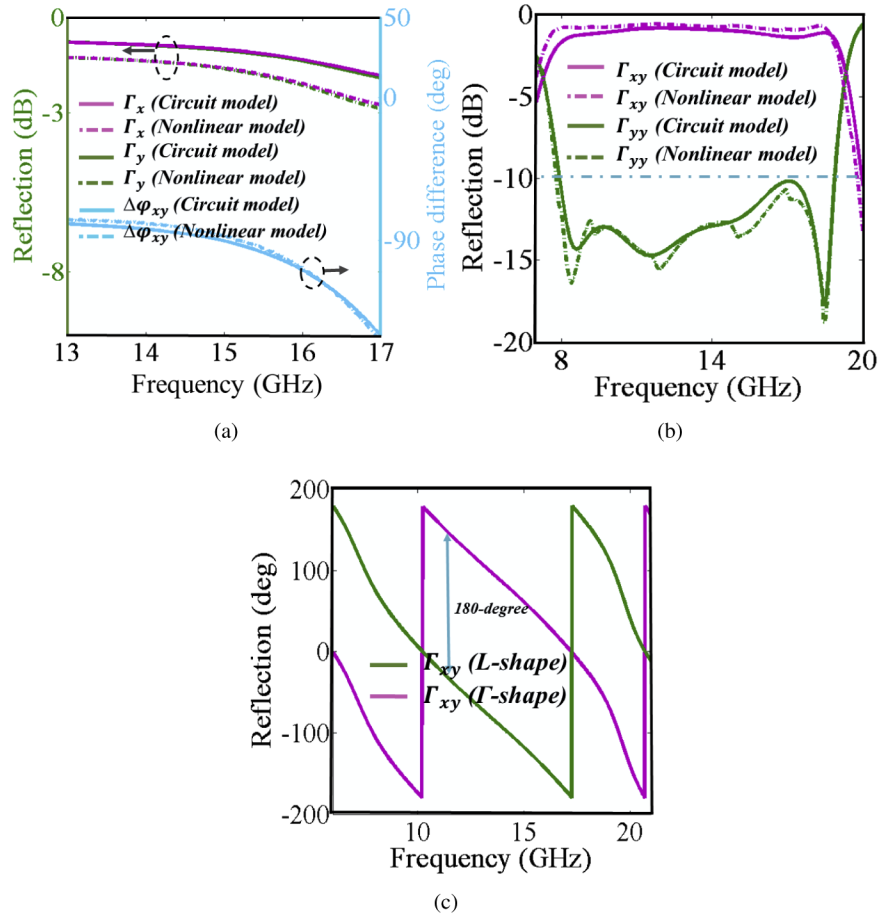
Fig. 3. (a) The simulated reflection coefficients Γ_x and Γ_y and their phase difference $\Delta\varphi_{yx}$ of the QWP with simplified *LC*-circuit and nonlinear (SPICE) model.(b) The simulated reflection coefficients Γ_{xy} and Γ_{yy} of the DSWMM with simplified *RL*-circuit model and nonlinear (SPICE) model(c) The simulated phase difference between L−shape and Γ-shape meta−atoms at high power intensities.

for linear polarization conversion at high power levels as follows:

$$AR = \sqrt{\frac{\frac{1}{r}\cos^2\alpha + \sin 2\alpha \cos\Delta\varphi_{xy} + r\sin^2\alpha}{\frac{1}{r}\sin^2\alpha - \sin 2\alpha \cos\Delta\phi_{xy} + r\cos^2\alpha}} \tag{2}$$

where

$$r = \frac{|\Gamma_x|}{|\Gamma_y|} \tag{3}$$

and

$$2\alpha = \tan^{-1}\left(\frac{2r}{1-r^2}\right)\cos\Delta\varphi_{xy} \tag{4}$$

$$PCR = \frac{\Gamma_{xy}^2}{\Gamma_{yy}^2 + \Gamma_{xy}^2} \tag{5}$$

Figure 4(a) shows the AR and PCR of the L−shape and Γ−shape meta−atoms at low power levels as a QWP and as a DSWMM at high power levels, respectively. It is clearly seen the AR

better than 3 dB over 21.2% from 13.24 GHz to 16.38 GHz and PCR better than 0.8 over 81.4% from 8.12 GHz to 19.27 GHz. In addition, we study the effect of oblique incidence wave on polarization conversion at different power levels. Figure 4(b) illustrates at low power intensities, altering the incidence angle from $\theta = 0°$ to $30°$ contributes to the shifting in the LP-to-CP bandwidth. On the other hand, at high power intensities, by increasing the incidence angle from $\theta = 0°$ to $30°$, the PCR bandwidth slightly starts to decreasing (see Fig. 4(c)). Table 1 presents a comparison among the proposed nonlinear converter and other reported diode-based polarization converters. The comparison shows that the proposed converter not only can nonlinearly do LP-to-CP and LP-to-LP polarization conversion but also has an ultrawide frequency band in which the PCR for linear polarization conversion and AR for circular polarization are greater than 80% and 20% respectively.
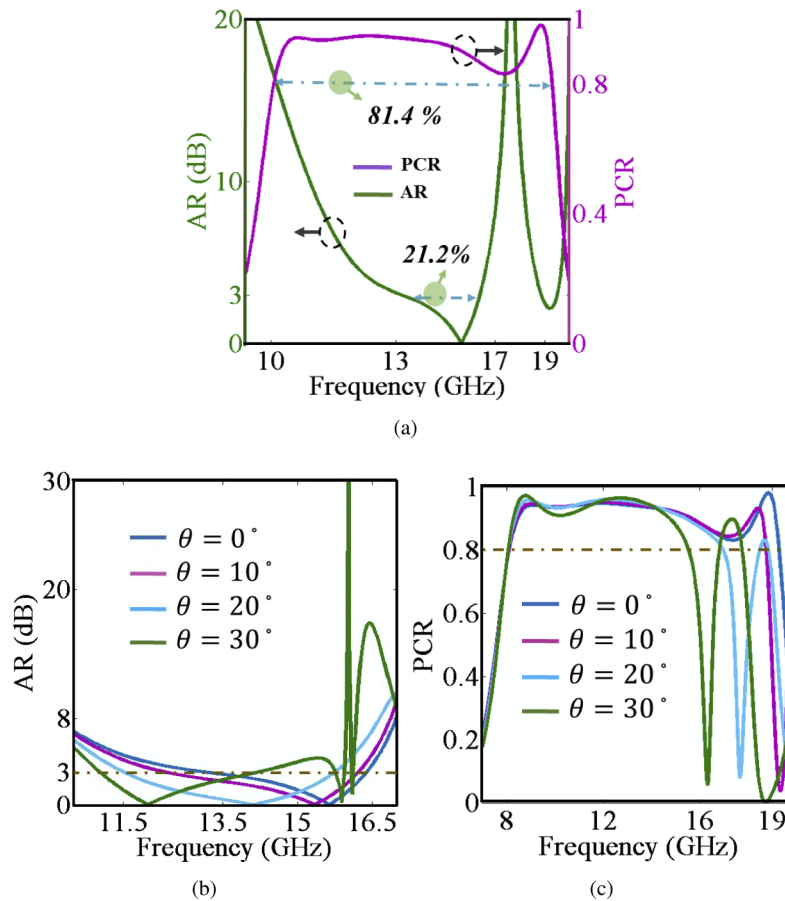

(a)

(b)

(c)

Fig. 4. (a) The calculated PCR for linear polarization conversion at high power intensities and AR for circular polarization conversion at low power intensities. The simulated (b) PCR and (c) AR at oblique incident of EM waves (equals 0°, 10°, 20°, and 30°).

To justify the LP-to-RHCP performance of the metasurface at low power intensities, when PIN-diodes are in off mode, the electric field intensity distribution of the L−shape and Γ−shape unit cells along with phase at 14 GHz has been shown in Figs. 5(a) and 5(b). By increasing the phase, the yellow part on the top layer of the unit cells rotates counterclockwise that results in the radiation of RHCP waves. To further understand the working mechanism of the metasurface as the ultrawideband linear-to-linear polarizer at high power levels, the surface current of the

Table 1. Comparison with other reconfigurable polarization converters.

	Biasing	LP-to-CP	LP-to-LP	Bandwidth (%)
Ref [24]	DC	✗	✓	1.1
Ref [43]	DC	✓	✗	1.6
Ref [44]	DC	✓	✗	8
Ref [45]	DC	✗	✓	62-71
Ref [46]	DC	✓	✓	49.1-67.8
Present Study	AC	✓	✓	21.2-81.4

meta−atoms and ground planes at 8.6 GHz, 11.5 GHz, 15 GHz, and 18.5 GHz as resonance frequencies are depicted in Figs. 6(a)–6(d) and Figs. 7(a)–7(d). At 8.6 GHz and 11.5 GHz, the meta−atoms currents and ground plane currents are anti-parallel; these loop currents have resulted in magnetic resonances. Conversely, at 15 and 18.5 GHz, the parallel currents flowing between meta−atoms and ground plane have generated electric resonances. By optimizing the structural parameters, the multi-resonance metasurface can operate as an LP-to-LP polarization converter at high incident power levels in an ultra-wide frequency range [47].
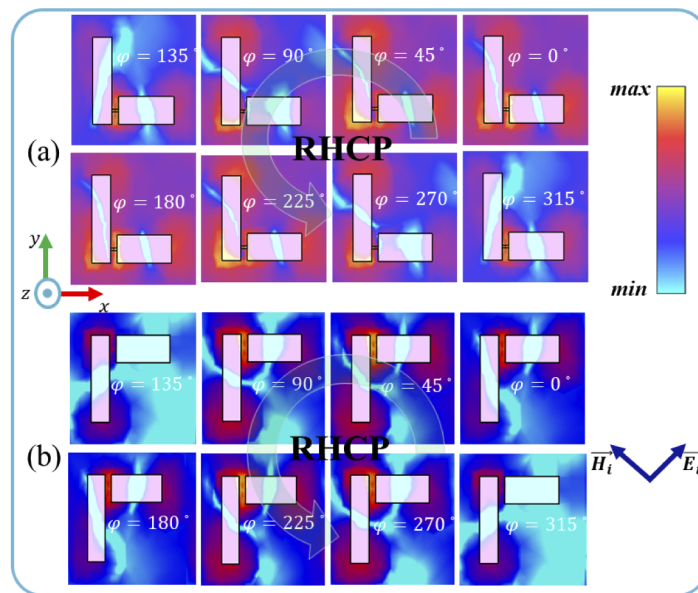

Fig. 5. Electric field distributions of (a) L−shape (b) Γ−shape meta−atoms at low power intensities when PIN-diodes are in off mode at 14 GHz.

2.3. Nonlinear analysis

The use of PIN-diodes as the nonlinear elements may contribute to harmful effects such as harmonic generation, third-order inter-modulation and AM modulation on fundamental frequency. Therefore, to check the validity of the structure, nonlinear analysis is essential. In this regard, the scattering parameters of the L−shape and Γ−shape meta−atoms, in the form of an S3P file is imported to Advanced Design System (ADS) as a circuit-based nonlinear simulator. The S3P file consists of three ports: (1), (2) the first and second Floquet ports, and (3) a discrete port instead of the PIN-diode. In the ADS medium, the discrete port is occupied with the SPICE model of a Flip Chip diode (see Fig. 2(d)) with a serial number of MADP-000907-14020. In ADS
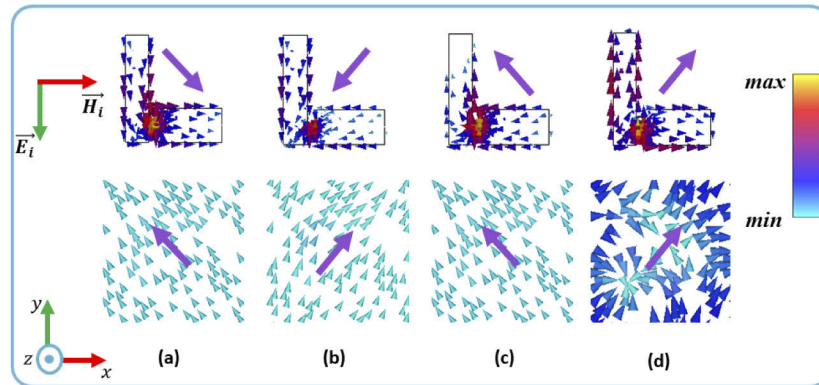
Fig. 6. Surface current distribution on the L−shape meta−atoms when PIN-diodes are in on mode at (a) 8.6 GHz, (b) 11.5 GHz, (c) 15 GHz, and (d) 18.5 GHz.
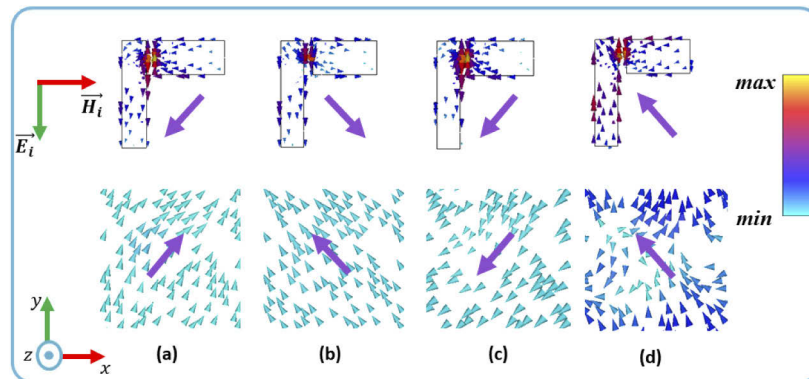

Fig. 7. Surface current distribution on the Γ−shape meta−atoms when PIN-diodes are in on mode at (a) 8.6 GHz, (b) 11.5 GHz, (c) 15 GHz, and (d) 18.5 GHz.

as an EM-circuit simulator, using the transient solver at 10 GHz frequency and two employed probes at both ends of the PIN-diode the AC voltage of the diode at different power levels has been measured. As can be seen in Fig. 8(a), when small signals illuminate the meta−atoms, the diode voltages is a complete sinusoidal curve. By contrast, the illuminated large signals generate distorted voltage wave-forms so that the positive half cycles are truncated to the diode forward voltage (1.3 V). The threshold impinged power of off-to-on switching is obtained 3 dBm for each 10.6 mm × 10.6 mm unit cell. For the proposed metasurface that composed of 576 unit cells, the minimum impinging power to switch the state of diodes from off-to-on is calculated 30.06 dBm, therefore, the metasurface at this power as a self-biased nonlinear surface without needs to a complex DC biasing network could switch its functionality from a QWP to a DSWMM. Again, it must be mentioned that at high frequencies for high power illuminations since the carriers injecting rate to the intrinsic layer during the positive cycles is much more than the carriers outgoing rate from the intrinsic layer during the negative cycles, despite the time variations of the induced voltage, the operational status of the diodes would be stable [37].

As mentioned before, one of the harmful effects of using nonlinear devices such as PIN-diodes may be the generation of frequency harmonics. Hence, A harmonic balance analysis using ADS software to more study the nonlinear behavior of the integrated meta−atom with PIN-diode is done. In this case, one of the Floquet ports is excited with a 15 dBm signal, and the power at
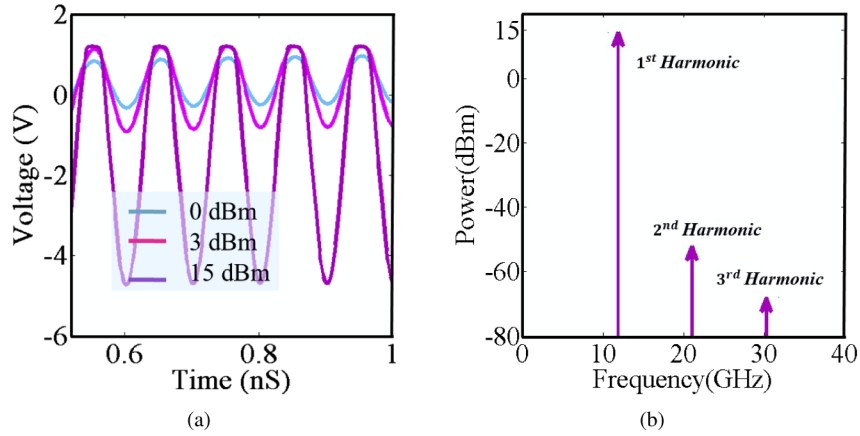
Fig. 8. (a) Induced voltage at both ends of one PIN-diode. (b) The Harmonic Balance analysis for a 15 dBm signal at 11 GHz.

another port is measured. As we expected the most parts of the input power has appeared in the second Floquet port (cross-polarization) at the fundamental frequency here 11 GHz (see Fig. 8(b)). As a result, the nonlinear analyzes (LSSP, Transient Response and Harmonic balance) with EM-circuit simulator validate our assumption in the modelling of PIN-diode for full-wave simulations.

3. Discussion

As shown in the schematic diagram of the proposed metasurface (Fig. 1), at high power intensities, the distribution of the L−shape and Γ−shape anti-phase meta−atoms as the coding particles over the metasurface spatially manipulates the incoming wave. The nonlinear metasurface as a DSWMM contains 6×6 binary super-cells such that each super-cell is composed of 4×4 L−shape or Γ−shape meta−atoms to depreciate defective corner-related coupling effects between the neighboring super-cells. The far field pattern function of the DSWMM can be expressed by a superposition from the contributions of all super-cells.

$$E^{\text{far}}(\theta, \varphi) = f_e(\theta, \varphi) \sum_{m=1}^{N} \sum_{n=1}^{N} exp\left(-i\{\varphi_{mn} + kDsin\theta\left[(m-1/2)cos\varphi + (n-1/2)sin\varphi\right]\}\right) \quad (6)$$

where, $f_e(\theta, \varphi)$ is the pattern function of a super-cell, and θ and φ denote to the elevation and azimuth angles, respectively. D remarks the period of the digital super-cells along both x- and y−directions, and $k = 2\pi/\lambda$ refers to the free-space wave-number. Referring to the above equation, if we consider a quasi-omnidirectional far-field pattern for all super-cells, the realized scattering patterns of different coding configurations can be expressed in the forms of two-dimensional inverse Fourier transforms of the super-cells, i.e., $E^{far}(\omega_1, \omega_2) = F^{-1}(u_{mn})$. Here, ω_1 and ω_2 remark the spatial Fourier space variables, and u_{mn} is the complex status of each super-cell [48].

Based on the generalized Snell's law [49], the scattering direction of the DSWMM in spherical coordinates (θ, φ) can be determined using the following relations:

$$\varphi_1 = \pm tan^{-1}\frac{D_x}{D_y}, \quad \varphi_2 = \pi \pm tan^{-1}\frac{D_x}{D_y} \quad (7)$$

$$\theta = sin^{-1}(\lambda\sqrt{\frac{1}{D_x^2} + \frac{1}{D_y^2}}) \quad (8)$$

in which, D_x and D_y indicate the spatial periods of the coding sequence along the $x-$ and $y-$axis, respectively. In Figs. 8(a) and 8(b) and Figs. 9(a) and 9(b), the normalized two-dimensional (2D) and 3D scattering pattern of the two conventional coding configurations 010101. . ./010101. . . (stripped configuration) and 010101. . ./101010. . . (chessboard configuration) at 12.6 GHz are sketched, respectively. For sequence 1, where D_x is infinite and D_y is 80 mm, two symmetric reflected beams with directions $(\theta_1, \phi_1)=(17.3°,0°)$ and $(\theta_2, \phi_2)=(17.3°,180°)$ are achieved; similarly, for chessboard configuration, four symmetric reflected beams with directions $(\theta_1, \phi_1)=(25°,45°)$, $(\theta_2, \phi_2)=(25°,135°)$, $(\theta_3, \phi_3)=(25°,225°)$, and $(\theta_4, \phi_4)=(25°,315°)$ are obtained. The numerical results in Figs. 9(a) and 9(b) are obtained with the help of CST Microwave Studio, which is consistent with theoretical predictions. The use of randomness distribution of the coding particles gives rise to lower scattering signatures over a broad frequency range from X-band to Ku-band. Hence, we use an entropy-based method to reach the efficient diffusion-like scattering pattern for smart camouflage surface applications. Entropy as a key gauge to describe the information of different types of coding configuration Can be accepted [50]. Surely, the more average entropy measure, as well as diffusion level, results in the lower probability of estimation of scattering patterns. In [51], the authors have validated the ability of the 2D quadratic Renyi entropy to reach the best diffusion-like coding configuration. According to the high ability of the Renyi entropy in measuring Gaussianity in the 2D scattering pattern, it could be utilized to interpret different coding configurations. Herein, Binary Bat Algorithm (BBA) as a fast, simple, and efficient optimization method in comparison to the conventional optimization methods to reach the best diffusion phase-encoded pattern has been used that its relation can be expressed as:

$$H_{Re} = \max\left\{ \frac{-1}{2}\log\left[\sum_{i=1}^{128}\sum_{i_R=1}^{128} P_{ii_R}^2 + \sum_{i=1}^{128}\sum_{i_R=1}^{128} P_{ii_D}^2 \right] \right\} \tag{9}$$

here, P_{ii_R} and P_{ii_D} remark the ii_R and ii_D indexes in PDF$_{JR}$ and PDF$_{JD}$ diagrams, respectively. These two PDF diagrams based on the statuses of each neighbouring pair of the 2D-IFFT image matrix elements in the vertical and horizontal directions can be determined. The Renyi entropy for different distribution of L−shape Γ−and shape meta−atoms as the anti-phase coding particles is calculated and shown in Table 2. In addition, with the help of Binary Bat Algorithm (BBA) the optimal diffusion coding configuration to reach the maximum entropy, as well as the maximum diffusion among all potential solutions, is achieved. In this case, the quantity of the H_{Re} is calculated as high as 1.80. As can be seen in Fig. 10(c), the high power incident waves are scattered along with the numerous random directions by the entropy-based randomized coding metasurface in such a way no main scattered lobes exist. As an application, this nonlinear metasurface can reduce both bi-static and mono-static RCS (see Fig. 10(d)) for high power incident waves. The numerical simulations clarify the significance of this work at the microwave band among all of the nonlinear metasurfaces that recently are introduced. Unlike previous works, the metasurface according to the power level of the incoming waves controls and manipulates them over 21.2% (low power signals) and 81.4% (high power signals) bandwidths.

Table 2. The computed Renyi entropy for different distribution of coding particles.

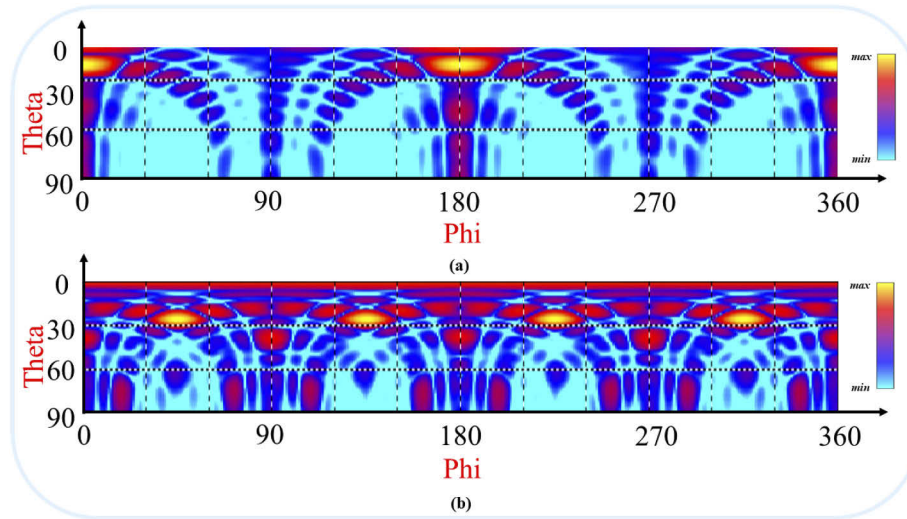| Coding configuration	Renyi entropy(H_{Re})
PEC reflector	0.143
Stripped configuration	0.318
Chessboard configuration	0.452
Optimal Diffusion configuration	1.80

Fig. 9. The 2-D far-field results that show the performance of the metasurface upon illuminating by high-power incidences for (a) stripped configuration and (b) Chessboard configuration.
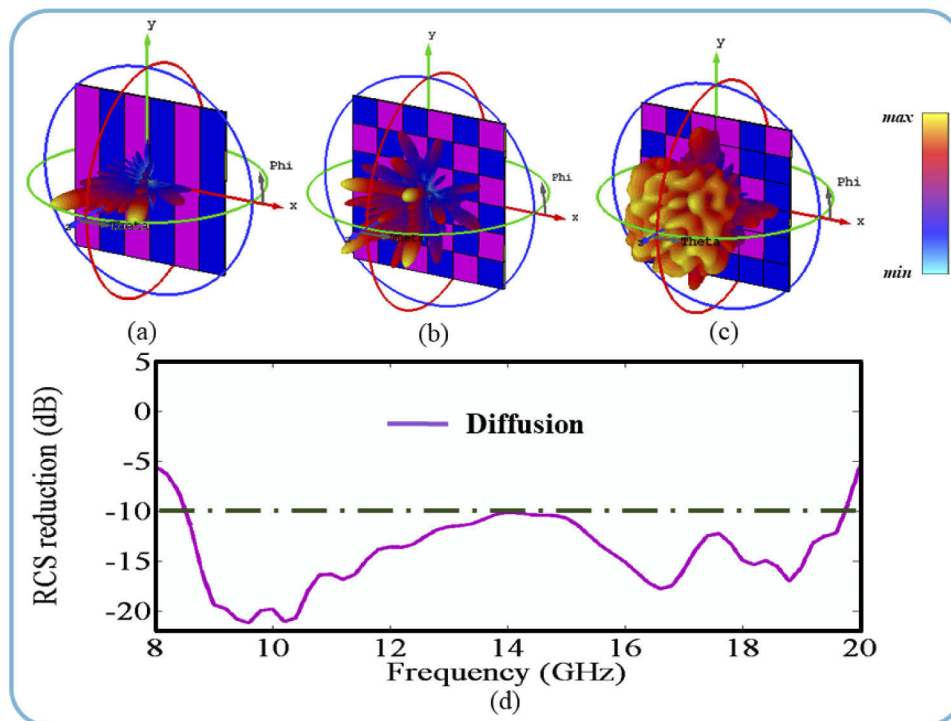

Fig. 10. The 3-D simulation patterns of the nonlinear metasurface as a DSWMM, which indicate its ability to manipulate reflection waves using various coding sequences under the normal incidence of EM waves at center frequency 14 GHz. (a) stripped, (b) Chessboard, and (c) the optimal diffusion configurations. (d) The ability of the randomized coding pattern at high power intensities in RCS reduction relative to the same-sized copper plate.

4. Conclusion

We proposed a passive wideband self-biased nonlinear reflective metasurface at microwave frequencies to spatially control electromagnetic waves. The designed metasurface is composed of L−shape and Γ− shape meta−atoms that loaded with self-biased PIN-diode elements. The EM functionality of the passive structure is determined by the level of incident power so that at low power intensities, the nonlinear metasurface as an anisotropic surface acts as a QWP, changes the linear polarization of the incoming wave to the circular polarization. On the other hand, the multi-resonant characteristic of the nonlinear metasurface at high power intensities causes the linear polarization of the incident wave converts to cross-polarization. Moreover, using the anti-phase meta−atoms with same magnitudes results to a digital metasurface. Then, an entropy-based binary coding pattern and Binary Bat Optimization Algorithm are mixed to obtain a diffusion-like far-field pattern over a broad frequency range. Nonlinear circuit-based analyzes in addition to the full-wave simulations verified the powerful wave control ability of the nonlinear metasurface.

Disclosures

The authors declare no conflicts of interest.

References

1. R. A. Shelby, D. R. Smith, and S. Schultz, "Experimental verification of a negative index of refraction," Science **292**(5514), 77–79 (2001).
2. R. W. Ziolkowski, "Design, fabrication, and testing of double negative metamaterials," IEEE Trans. Antennas Propag. **51**(7), 1516–1529 (2003).
3. R. W. Ziolkowski, P. Jin, and C.-C. Lin, "Metamaterial-inspired engineering of antennas," Proc. IEEE **99**(10), 1720–1731 (2011).
4. M. Movahhedi and N. Komjani, "Dual-frequency dual orthogonal polarization wave multiplexing using decoupled pixels based on holographic technique," Opt. Express **28**(8), 12424–12438 (2020).
5. M. Movahhedi, M. Karimipour, and N. Komjani, "Multibeam bidirectional wideband/wide-scanning-angle holographic leaky-wave antenna," IEEE Antennas Wirel. Propag. Lett. **18**(7), 1507–1511 (2019).
6. M. M. Moeini, H. Oraizi, and A. Amini, "Collimating cylindrical surface leaky waves for highly improved radiation characteristics of holograms," Phys. Rev. Appl. **11**(4), 044006 (2019).
7. J. B. Pendry, D. Schurig, and D. R. Smith, "Controlling electromagnetic fields," Science **312**(5781), 1780–1782 (2006).
8. J. Li and J. B. Pendry, "Hiding under the carpet: a new strategy for cloaking," Phys. Rev. Lett. **101**(20), 203901 (2008).
9. M. Rahmanzadeh, H. Rajabalipanah, and A. Abdolali, "Multilayer graphene-based metasurfaces: robust design method for extremely broadband, wide-angle, and polarization-insensitive terahertz absorbers," Appl. Opt. **57**(4), 959–968 (2018).
10. Y. Zhao and A. Alù, "Manipulating light polarization with ultrathin plasmonic metasurfaces," Phys. Rev. B **84**(20), 205428 (2011).
11. Q. Feng, M. Pu, C. Hu, and X. Luo, "Engineering the dispersion of metamaterial surface for broadband infrared absorption," Opt. Lett. **37**(11), 2133–2135 (2012).
12. Y. Guo, Y. Wang, M. Pu, Z. Zhao, X. Wu, X. Ma, C. Wang, L. Yan, and X. Luo, "Dispersion management of anisotropic metamirror for super-octave bandwidth polarization conversion," Sci. Rep. **5**(1), 8434 (2015).
13. A. Babaee, A. Momeni, A. Abdolali, and R. Fleury, "Parallel optical computing based on mimo metasurface processors with asymmetric optical response," arXiv preprint arXiv:2004.02948 (2020).
14. A. Momeni, H. Rajabalipanah, A. Abdolali, and K. Achouri, "Generalized optical signal processing based on multioperator metasurfaces synthesized by susceptibility tensors," Phys. Rev. Appl. **11**(6), 064042 (2019).
15. A. Abdolali, A. Momeni, H. Rajabalipanah, and K. Achouri, "Parallel integro-differential equation solving via multi-channel reciprocal bianisotropic metasurface augmented by normal susceptibilities," New J. Phys. **21**(11), 113048 (2019).
16. H. Rajabalipanah, A. Abdolali, S. Iqbal, L. Zhang, and T. J. Cui, "How do space-time digital metasurfaces serve to perform analog signal processing?" arXiv preprint arXiv:2002.06773 (2020).
17. A. Momeni, M. Safari, A. Abdolali, and N. P. Kherani, "Tunable and dynamic polarizability tensor for asymmetric metal-dielectric super-cylinders," arXiv preprint arXiv:1904.04102 (2019).
18. K. Rouhi, A. Abdolali, and S. Fallah, "Wideband thz low-scattering surface based on combination of diffusion and absorption," arXiv preprint arXiv:2001.09289 (2020).

19. A. Fallahi and J. Perruisseau-Carrier, "Design of tunable biperiodic graphene metasurfaces," Phys. Rev. B **86**(19), 195408 (2012).

20. H. Cheng, S. Chen, P. Yu, W. Liu, Z. Li, J. Li, B. Xie, and J. Tian, "Dynamically tunable broadband infrared anomalous refraction based on graphene metasurfaces," Adv. Opt. Mater. **3**(12), 1744–1749 (2015).

21. L. Liu, L. Kang, T. S. Mayer, and D. H. Werner, "Hybrid metamaterials for electrically triggered multifunctional control," Nat. Commun. **7**(1), 13236 (2016).

22. S. Cueff, D. Li, Y. Zhou, F. J. Wong, J. A. Kurvits, S. Ramanathan, and R. Zia, "Dynamic control of light emission faster than the lifetime limit using vo 2 phase-change," Nat. Commun. **6**(1), 8636 (2015).

23. M. R. M. Hashemi, S.-H. Yang, T. Wang, N. Sepúlveda, and M. Jarrahi, "Electronically-controlled beam-steering through vanadium dioxide metasurfaces," Sci. Rep. **6**(1), 35439 (2016).

24. B. Ratni, A. de Lustrac, G.-P. Piau, and S. N. Burokur, "Electronic control of linear-to-circular polarization conversion using a reconfigurable metasurface," Appl. Phys. Lett. **111**(21), 214101 (2017).

25. L. Li, T. J. Cui, W. Ji, S. Liu, J. Ding, X. Wan, Y. B. Li, M. Jiang, C.-W. Qiu, and S. Zhang, "Electromagnetic reprogrammable coding-metasurface holograms," Nat. Commun. **8**(1), 197 (2017).

26. A. Rose, D. A. Powell, I. V. Shadrivov, D. R. Smith, and Y. S. Kivshar, "Circular dichroism of four-wave mixing in nonlinear metamaterials," Phys. Rev. B **88**(19), 195148 (2013).

27. A. Rose, D. Huang, and D. R. Smith, "Controlling the second harmonic in a phase-matched negative-index metamaterial," Phys. Rev. Lett. **107**(6), 063902 (2011).

28. W. Ye, F. Zeuner, X. Li, B. Reineke, S. He, C.-W. Qiu, J. Liu, Y. Wang, S. Zhang, and T. Zentgraf, "Spin and wavelength multiplexed nonlinear metasurface holography," Nat. Commun. **7**(1), 11930 (2016).

29. C. Zhao, C.-F. Wang, and S. Aditya, "Power-dependent frequency-selective surface: Concept, design, and experiment," IEEE Trans. Antennas Propag. **67**(5), 3215–3220 (2019).

30. H. Wakatsuchi, S. Kim, J. J. Rushton, and D. F. Sievenpiper, "Circuit-based nonlinear metasurface absorbers for high power surface currents," Appl. Phys. Lett. **102**(21), 214103 (2013).

31. T. J. Cui, M. Q. Qi, X. Wan, J. Zhao, and Q. Cheng, "Coding metamaterials, digital metamaterials and programmable metamaterials," Light: Sci. Appl. **3**(10), e218 (2014).

32. K. Rouhi, H. Rajabalipanah, and A. Abdolali, "Real-time and broadband terahertz wave scattering manipulation via polarization-insensitive conformal graphene-based coding metasurfaces," Ann. Phys. **530**(4), 1700310 (2018).

33. K. Rouhi, H. Rajabalipanah, and A. Abdolali, "Multi-bit graphene-based bias-encoded metasurfaces for real-time terahertz wavefront shaping: From controllable orbital angular momentum generation toward arbitrary beam tailoring," Carbon **149**, 125–138 (2019).

34. Z. Luo, Q. Wang, X. G. Zhang, J. W. Wu, J. Y. Dai, L. Zhang, H. T. Wu, H. C. Zhang, H. F. Ma, Q. Cheng, and T. J. Cui, "Intensity-dependent metasurface with digitally reconfigurable distribution of nonlinearity," Adv. Opt. Mater. **7**(19), 1900792 (2019).

35. Z. Luo, M. Z. Chen, Z. X. Wang, L. Zhou, Y. B. Li, Q. Cheng, H. F. Ma, and T. J. Cui, "Digital nonlinear metasurface with customizable nonreciprocity," Adv. Funct. Mater. **29**(49), 1906635 (2019).

36. Z. Wu, M. Lin, J. Liu, and J. Zhang, "Waveguide energy-selection-filter switch array," IEEE Access **7**, 67686–67694 (2019).

37. Z. Wu, M. Lin, J. Zhang, and J. Liu, "Energy selective filter with power-dependent transmission effectiveness in waveguide," Electronics (Basel, Switz.) **8**(2), 236 (2019).

38. C. Zhao and C.-F. Wang, "A power dependent frequency selective surface," in *2017 IEEE International Symposium on Antennas and Propagation & USNC/URSI National Radio Science Meeting*, (IEEE, 2017), pp. 1029–1030.

39. M. Kiani, M. Tayarani, A. Momeni, H. Rajabalipanah, and A. Abdolali, "Self-biased tri-state power-multiplexed digital metasurface operating at microwave frequencies," Opt. Express **28**(4), 5410–5422 (2020).

40. H. Yang, X. Cao, F. Yang, J. Gao, S. Xu, M. Li, X. Chen, Y. Zhao, Y. Zheng, and S. Li, "A programmable metasurface with dynamic polarization, scattering and focusing control," Sci. Rep. **6**(1), 35692 (2016).

41. L. A. Coldren, S. W. Corzine, and M. L. Mashanovitch, *Diode lasers and photonic integrated circuits*, vol. 218 (John Wiley & Sons, 2012).

42. M. Yoo and S. Lim, "Active metasurface for controlling reflection and absorption properties," Appl. Phys. Express **7**(11), 112204 (2014).

43. W. Li, S. Gao, Y. Cai, Q. Luo, M. Sobhy, G. Wei, J. Xu, J. Li, C. Wu, and Z. Cheng, "Polarization-reconfigurable circularly polarized planar antenna using switchable polarizer," IEEE Trans. Antennas Propag. **65**(9), 4470–4477 (2017).

44. W. Li, S. Xia, B. He, J. Chen, H. Shi, A. Zhang, Z. Li, and Z. Xu, "A reconfigurable polarization converter using active metasurface and its application in horn antenna," IEEE Trans. Antennas Propag. **64**(12), 5281–5290 (2016).

45. Y. Li, Y. Wang, and Q. Cao, "A reflective multilayer polarization converter with switchable frequency band," J. Appl. Phys. **127**(4), 045301 (2020).

46. X. Gao, W. L. Yang, H. F. Ma, Q. Cheng, X. H. Yu, and T. J. Cui, "A reconfigurable broadband polarization converter based on an active metasurface," IEEE Trans. Antennas Propag. **66**(11), 6086–6095 (2018).

47. X. Gao, X. Han, W. Cao, H. O. Li, H. F. Ma, and T. J. Cui, "Ultrawideband and high-efficiency linear polarization converter based on double v-shaped metasurface," IEEE Trans. Antennas Propag. **63**(8), 3522–3530 (2015).

48. H. Rajabalipanah and A. Abdolali, "Ultrabroadband monostatic/bistatic rcs reduction via high-entropy phase-encoded polarization conversion metasurfaces," IEEE Antennas Wirel. Propag. Lett. **18**(6), 1233–1237 (2019).

49. N. Yu, P. Genevet, M. A. Kats, F. Aieta, J.-P. Tetienne, F. Capasso, and Z. Gaburro, "Light propagation with phase discontinuities: generalized laws of reflection and refraction," Science **334**(6054), 333–337 (2011).
50. L. Golshani, E. Pasha, and G. Yari, "Some properties of rényi entropy and rényi entropy rate," Inf. Sci. **179**(14), 2426–2433 (2009).
51. A. Momeni, K. Rouhi, H. Rajabalipanah, and A. Abdolali, "An information theory-inspired strategy for design of re-programmable encrypted graphene-based coding metasurfaces at terahertz frequencies," Sci. Rep. **8**(1), 6200 (2018).